

Graphene-Based BPSK and QPSK Modulators Working at A Very High Bit Rate (Up Tbps Range)

Almir Wirth Lima Junior (✉ awljeng@gmail.com)

Instituto Federal de Educacao Ciencia e Tecnologia do Ceara <https://orcid.org/0000-0001-5988-6190>

Wilton Bezerra-Fraga

Federal Institute of Education Science and Technology of Ceara: Instituto Federal de Educacao Ciencia e Tecnologia do Ceara

Research Article

Keywords: BPSK, Graphene, Modulator, QPSK

Posted Date: February 15th, 2021

DOI: <https://doi.org/10.21203/rs.3.rs-194687/v1>

License: © ⓘ This work is licensed under a Creative Commons Attribution 4.0 International License.

[Read Full License](#)

Graphene-based BPSK and QPSK modulators working at a very high bit rate (up Tbps range)

A. J. Wirth-Lima ^{*1}, and W. Bezerra-Fraga ^{1,2}

*Corresponding author: awljeng@gmail.com

1 - Department of Physics, Federal Institute of Education, Science and Technology
of Ceará - Campus Sobral, Ceará, Brazil.

2 - Postgraduate Program in Electrical Engineering and Computing - Federal
University of Ceará (U.F.C.) - Sobral, Ceará, Brazil.

Abstract

We are presenting graphene-based Binary Phase Shift Keying (BPSK) and Quadrature Phase Shift Keying (QPSK) modulators, which can operate in the range from the TeraHertz up to the infrared. It is noteworthy that these devices have huge advantages over the silicon Mach-Zehnder optical modulators (MZMs) with lateral PN-junction rib-waveguide phase shifters. Among the countless advantages, we can mention, for example, that these modulators consist of only one waveguide and have a much simpler application system of the modulator signal (gate voltage) than in silicon-based MZMs. Other huge advantages are greater efficiency, and yet, they are cheaper and have shorter lengths (and consequently, greater integration in photonic integrated circuit (PIC)). The first step to present these modulators was to detail the graphene theory that is involved in this device. After this step, we show the project, numerical simulations, and analyses related to our graphene-based BPSK and QPSK modulators. We believe that these modulators will contribute to the generation of new devices made up of 2D materials, which should revolutionize this area of science.

Keywords: BPSK, Graphene, Modulator, QPSK.

1. Introduction

Coherent optical modulations, i.e., techniques of light modulations propagating in optical fibers using modulations of the amplitude, frequency, and phase of electromagnetic radiation, as well as signal transmission in two polarizations, were widely researched in the 1980s. It is worth mentioning that a receiver for extract the information contained in the phase modulations is termed as a coherent receiver.

The interest in these studies was because fiber optic links using coherent modulations can support longer lengths than links where are used OOK (On-Off-Keying) modulations without the use of optical amplifiers. It is noteworthy that in addition to the advantages mentioned above, frequency and phase modulation techniques can provide huger noise immunity. However, as since the 1990s, wavelength-division multiplexed (WDM) systems have been used, the amount of this type of research has decreased. It is noteworthy that WDM systems use conventional modulations (intensity-modulation and direct-detection - IMDD), as well as erbium-doped fiber amplifiers, which provides links with greater bandwidth and length [1] than standard optical fiber links. On the other hand, the increase of the bandwidth of optical fibers with coherent modulation (from the 2000s onwards) has led to a large number of researches related to this type of modulation. Then, the acquisition of transmitters and receivers (transceivers) of optical signals modulated in phase shift (Binary Phase Shift Keying - BPSK), as well as, in amplitude and phase shift in quadrature (quadrature phase-shift keying - QPSK), provided the development of these types of coherent modulations. A further advance in this regard was the use of optical delay to obtain the called differential quadrature phase-shift keying optical modulation - DQPSK [2]. In researches regarding QPSK modulations, the achievement of twice the bit rate, using that same transmission rate for symbols (symbol rate), so that, for example, a bit rate of 40 Gbps/s has been obtained from a symbol rate of 20 Gsymbol/s.

A high-speed monolithic Mach-Zehnder optical modulator was used in a coherent optical channel based on polarization-multiplexed quadrature-phase (DP-QPSK) with a bit rate of 128 Gb/s, for each wavelength channel, in a 1000 km long single-mode fiber link [3].

It is worth noting that, currently, in coherent optical channels, modulators consisting of silicon lateral PN-junction rib-waveguide phase shifters are used (Figure 1).

(Figure 1)

That occurs because the effective refractive index and the absorption coefficient of the silicon waveguides can be controlled, by changing the concentration of free-carriers

(holes and electrons), i.e., by plasma dispersion effect. In this type of optical signal modulation, a reverse electrical voltage and a modulating signal are applied at the PN junctions. Hence, the arms (silicon rib-waveguides) of the Mach-Zehnder Interferometer (MZI) provide the expansion of the depletion zone, as well as the change of the density of free charges (electrons and holes), and the consequent modification of the refractive index value [4, 5, 6], as it is showed in Figure 1.

Note that a reverse continuous voltage, together with the modulating electrical signal, is applied in the PN junction of the two arms of the MZM. It is noteworthy that the modulating digital signal, shown in Figure 1, could be replaced by a radio frequency signal (RF). That occurs when, for example, the MZM operates in RF communications systems over optical fibers, i.e., on the so-called analog photonics links (APLs) [7].

As we can see by Figure 1, each rib-waveguide consists of a PN junction located in its center, where an n-silicon is in contact with strongly doped silicon (n+) in one of its sides. Likewise, a p-silicon is in touch with a p+-silicon, and the silicon layers, n+, and p+ are in contact with a metal electrode.

To obtain a phase modulation, the modulating electrical signal is transformed into a bipolar NRZ signal, so that bits with a positive voltage are applied to one of the arms of the MZI, and bits with negative voltage go to the other arm of the MZI. These signals, together with the reverse voltage, supply the voltages in the two arms of the MZI, in order to obtain the phase variation between the optical signals that propagate in the two arms of the MZI. Hence, as the variation in the refractive index of silicon occurs due to the plasma dispersion effect, there is a change in the value of the effective index (n_{eff}) of the propagating mode, which provides a change in the value of the signal phase, at the output of the waveguide. Therefore, changing the value of the refractive index of silicon alters the values of the effective refractive index of the optical modes that propagate in the arms of the MZM, causing a change in the propagation speed of these propagating modes, which, consequently, causes a phase difference between the optical signals at the MZM output [3, 8, 9, 10]. Indeed, the increase in the value of the refractive index is caused by increasing the reverse voltage, as in this case, the free charges move away from the depletion zone. On the other hand, the decrease in the value of the refractive index is

provided with the decrease in the reverse voltage, since in this case, more load carriers go to the depletion zone.

The voltage between the two arms of the MZI that provides a π -phase shift (V_π) determines the efficiency of the modulation, i.e., the lower the value $L \times V_\pi$ (where L is the length of the traveling wave electrode (TWE)), the greater the modulation efficiency.

Note in the upper part of Figure 1, the schematic representation of the simplified equivalent circuit of PN junctions for this push-pull operation for zero-chirp modulation, through a TWE. Generally, the lengths of the two arms of the MZM are of the same length (symmetrical MZM), to avoid the occurrence of greater insertion loss in the longer arm.

A disadvantage of this type of modulation is that the change in the refractive index occurs in a non-linear manner [4, 11], causing signal distortion, due to several factors. Therefore, in this type of modulation, the linearity of the phase shift and the minimization of the carrier-induced optical loss are of great importance for obtaining a good performance of the MZM [9]. Hence, the MZM has to be biased at the quadrature point ($\pi/2$), which can be achieved with a bias voltage $V_{\text{bias}} = V_\pi/2$ i.e., with a phase shifter of $\pi/2$. Note that, in this case, in one of the arms, the resultant voltage value due to the modulating signal can be null ($-V_\pi/2 + V_\pi/2$; bit 1), while in the other arm can be $-V_\pi/2 - V_\pi/2 = -V_\pi$ (bit 0), as we can see by Figure 1. Moreover, the traveling wave electrode must be designed to match the group velocity of electrical signal to the group velocity of the light. The velocity matching allows high-speed modulation required in the range from 40 to 100 Gb/s [6]. For most modulators mentioned above, the traveling wave electrode has lengths between 3 mm to 4 mm.

It is noteworthy that a single MZM shown above can be used for BPSK modulations. However, to obtain QPSK modulation, two nested MZMs are used, as it is shown in Figure 2 [adapted from 10]. This subject is detailed in section 3.

We are presenting BPSK and QPSK modulators consisting of graphene-based waveguides, which can replace PN-junction rib-waveguides, with huge advantages. That modulators consist of only one waveguide and one modulator signal application system, which is much simpler than in the MZMs mentioned above. In addition to being more efficient and cheaper, they have shorter lengths, and consequently, greater integration in photonic integrated circuits (PICs). This is possible because graphene has free electrons in plasmonic undulations so that to change its dielectric constant (and consequently its refractive index), the external voltage can be applied directly to graphene (gate voltage). Then, the change in the propagation constant of graphene occurs more quickly. It is worth

mentioning that to increase the efficiency concerning to the contact area with graphene, we replaced silica with h-BN (Hexagonal Boron Nitride).

This work is constituted as follows: In section 2, we detail the part of physics encompassing graphene, which is necessary for detailing the graphene-based modulators, which we are presenting. We detail the BPSK and QPSK modulators, showing the design, involved theory, analysis via numerical simulations, and advantages of these modulators, in section 3. We close this manuscript, where the conclusions are (section 4).

2. Graphene

In order to be able to detail the BPSK and QPSK modulators consisting of graphene, we will show, in this section, the necessary theory regarding this 2D material.

The planar monolayer honeycomb lattice of graphene, consisting of two primitive lattice vectors, is shown in Figure 3.

(Figure 3)

It is worth noting the fact that for the most accurate possible determination of the lengths of graphene nanoribbons used in the devices we are presenting, it is necessary to take into account the distance between the carbon atoms in their atomic structure. As the lateral ends of the graphene are of the zigzag type, the lengths of the nanowires are a multiple of 0.123 nm.

2.1 Physical parameters for the graphene used in our nanophotonic modulator

In this section, we show the Equations that determine the operation of graphene and the respective control of the modulator we are presenting.

Optical conductivity of graphene

After some mathematical manipulations, we can arrive at the mathematical expressions that determine the intraband and interband conductivity of graphene ($\sigma_g = \sigma_{\text{intra}} + \sigma_{\text{inter}}$), given by [12, 16]:

$$\sigma_{\text{intra}}(\omega, \mu) = \frac{ie^2\mu_g}{(\omega+i\tau^{-1})\pi\hbar^2}; \quad 1$$

$$\sigma_{\text{inter}}(\omega, \mu) = \frac{e^2}{4\hbar} \left[1 + \frac{i}{\pi} \ln \frac{\hbar(\omega+i\tau^{-1})-2\mu_g}{\hbar(\omega+i\tau^{-1})+2\mu_g} \right], \quad 2$$

where

$$\mu_g \approx E_F \approx \hbar V_F \sqrt{n\pi}, \quad 3$$

is the graphene's chemical potential, E_F is the Fermi level, n is the charge density in graphene, $V_F = 1 \times 10^6$ m/s is the Fermi velocity, \hbar is the reduced Planck's constant, e is the electron charge, and w is the angular frequency.

It is noteworthy that τ is the electron relaxation time related to graphene, given by

$$\tau = \frac{\mu_m \mu}{e V_F^2}, \quad 4$$

μ_m being the charge mobility in graphene.

The charge density in graphene (n_{Vg}), which occurs due to the application of an external voltage (we will return to this subject later), is given by

$$n_{Vg} = \frac{\mu^2}{\hbar^2} \cdot \frac{1}{\pi V_F^2}. \quad 5$$

Note that for $\mu = 0$, $\sigma_{intra} = 0$, and $\sigma = \sigma_{inter} = \frac{e^2}{4\hbar} = \sigma_0$ (universal conductivity).

In the deduction of Equations 1 and 2, it was considered $\mu \gg K_B T$, being admitted that the ambient temperature is $T = 300$ K so that $K_B T \approx 26$ meV (K_B is the Boltzmann's constant, T is the temperature in Kelvin). Note that for $\mu = 0$, $\sigma_{intra} = 0$ and $\sigma = \sigma_{inter} = \frac{e^2}{4\hbar} = \sigma_0$ (universal conductivity).

To avoid losses due to the change in conductivity caused by interband transitions (first-order process), it is necessary to block these interactions by increasing the value related to the graphene's chemical potential. In this way, only surface plasmons polaritons in graphene (GSPPs) with a frequency above the limit, that is, $\hbar w_{inter} / \mu_g = 2 \rightarrow w_{inter} = 2\mu_g / \hbar$, suffer this type of attenuation [17].

Electrical permittivity of graphene

Considering the graphene's thickness $t = 0.34$ nm, its effective relative permittivity is given by:

$$\varepsilon_{rg}(w) = 1 - j \frac{\sigma}{w \varepsilon_0 t}. \quad 6$$

Furthermore, there is another Equation related to the effective relative permittivity, which takes into account the air impedance ($\eta_0 \approx 377 \Omega$), the photon wave number in the vacuum (k_0), as well as the conductivity of graphene, given by [15]:

$$\varepsilon_{rg} = 1 + \frac{j\sigma\eta_0}{k_0 t}. \quad 7$$

Using Equations 6 and 7 ($\mu_g = 0.55$ eV), we plotted the values of the graphene's dielectric constant, considering the graphene embedded in a Hexagonal Boron Nitride (h-

BN), and wavelength range $1.36 \mu\text{m} \leq \lambda \leq 1.625 \mu\text{m}$ (E, S, C, and L bands of ITU-T). Then, we found that the results were identical, according to what is showed in Figures 4a (real part) and 4b (imaginary part).

(Figure 4)

We considered that h-BN provides the mobility of graphene $\mu_m = 60000 \text{ cm}^2/\text{Vs}$, and we adopted the value 3.4 for its dielectric constant [18, 19, 20].

In Figures 4c and 4d, we can see the values for the graphene's dielectric constant, considering its chemical potential in the range $0.3 \text{ eV} \leq \mu_g \leq 0.9 \text{ eV}$ and wavelength $\lambda = 1.55 \mu\text{m}$.

Complementing the information we showed in this section, graphene can support TM modes, when $0 < \hbar\omega/\mu_g < 1.667$ ($\sigma'' > 0$) and TE modes, when $1.667 < \hbar\omega/\mu_g < 2$ ($\sigma'' < 0$) [21].

Wavenumber related to the wavevector in the direction of propagation (propagation constant) in a single layer of graphene

The complex wave number, in the direction of propagation, referring to a graphene nanoribbon embedded in a single dielectric to graphene, for GSPP TM modes is given by [14, 15]:

$$k_{c_TM} = k_0 \sqrt{\varepsilon_d - \left(\frac{2\varepsilon_d}{\sigma\eta_0}\right)^2}, \quad 8$$

where $\eta_0 = \sqrt{\mu_0/\varepsilon_0} \approx 377 \Omega$ is the intrinsic impedance of the free space.

On the other hand, for GSPP TE modes, the complex wave number in the direction of propagation for these referred GSPP TE modes is given by:

$$k_{c_TE} = k_0 \sqrt{\varepsilon_d - \left(\frac{\sigma\eta_0}{2\varepsilon_d}\right)^2}. \quad 9$$

Graphene nanoribbon working as a waveguide

GSPPs in a layer of graphene, acting as a waveguide, can be obtained through direct coupling between photons emitted by an optical emitter and surface plasmons (SPs) located on that layer. In a Research, it has been demonstrated that the optical emitter located on the same plane as the graphene layer (with polarization in the direction of the width of the graphene strip) provides coupling between photons emitted by the emitter and GSPPs, ten times greater than the emitter positioned over the graphene layer [22]. It

is noteworthy that the edge of the graphene nanoribbon ("armchair" or "zigzag") does not change the coupling process mentioned above [22].

GSPPs can occur in structures wider than 10 nm since, for dimensions below this value, plasmons occur into several resonances due to the characteristics of the carbon structures, as well as the quantum nature of their optical excitations [23].

Analysis of the occurrence of GSPPs modes in graphene nanoribbons with widths ranging from 25 nm to 100 nm made it possible to obtain a method to determine the dispersion ratios of the GSPPs, considering the energy of these modes [24].

The propagation length of the GSPPs modes (the distance that a GSPP mode travels, until it drops to $1/e$ from its initial intensity) is given by $L_p = 1/2 \text{Imag}(\beta)$ [14, 24].

We considered the graphene layer embedded between two layers of hexagonal boron nitride (h-BN). The reason for choosing h-BN is that the roughness of the h-BN layer is much less than that of the silica surface. Therefore, a graphene layer located between two layers of h-BN has much higher charge mobility and homogeneity than embedded in SiO_2 . Additionally, as there are few charge traps on the graphene/h-BN interface, the electronic properties of the device have much better values than on the graphene SiO_2 interface [20, 25]. The dielectric constant of h-BN has a value close to the SiO_2 (3.9). We have adopted $\epsilon_{\text{hBN}} = 3.4$ [19, 20, 25].

Gate voltage applied to a graphene waveguide

The two most used methods for obtaining control of the physical/optical parameters of graphene is through chemical doping [26, 27, 28] and via gate voltage.

An efficient way to controlling of the chemical potential of graphene is to use a gate voltage. For example, it is possible to localize the Fermi level for graphene in the valence band, applying a positive voltage to the graphene surface. On the other hand, the application of a negative voltage raises the Fermi level of graphene for the conduction band. It occurs because of the effect of the electric field so that the metallic electrode/h-BN/graphene region operates similarly to a capacitor [29, 30].

There are three ways to apply a gate voltage to graphene: back voltage, top voltage, and back/top voltage. Figure 5a shows an example of a scheme for obtaining a back gate voltage (V_{bg}) between silicon and a graphene nanoribbon. As we can see, the graphene nanoribbon was deposited on a substrate (in this case, silicon oxide) with a well-defined thickness, supported on highly doped silicon.

Taking into account that highly doped silicon works similarly to a metallic contact, silicon dioxide is insulating, and graphene is a zero-gap semimetal, we can say that an

electric field effect similar to that inside a capacitor of parallel plates occurs. Hence, it is possible to control the charge density in graphene through the application of gate voltage. We can use back gate voltage in graphene-based nanophotonic devices, such as, for example, a transistor, as we can see in Figure 5a (adapted from ref. [31]).

(Figure 5)

Therefore, the position of the Fermi level, whose value is practically the same as the chemical potential of graphene, can be controlled, in this case, through back gate voltage. Note that while applying a positive voltage to silicon (type p, highly doped) and a negative voltage to graphene causes electron transfer to graphene, and holes to silicon, applying a negative voltage to silicon, and a positive to graphene, occurs the transfer of holes to graphene and electrons to silicon.

It is worth noting that considering graphene as ideal, for $V_{bg} = 0$ eV, graphene would have minimal conductivity (σ_{min}), or maximum resistivity (ρ_{max}). However, in reality, considering real graphene, minimum conductivity does not occur in this condition because of the intrinsic doping of charges in graphene from the environment, and the device's manufacturing process, among other factors.

The value of the Dirac voltage (V_D), is defined as the value of the gate voltage where the minimum conductivity (or maximum resistivity) of graphene occurs. The influence in the value of Dirac voltage depends on graphene manufacturing and cleaning process, as well as the interface itself, in which there are energy levels that behave as acceptors/charge donors [32, 33]. Hence, the residual charge density value in graphene (n_0) is the range from $\approx 5 \times 10^{10} \text{ cm}^{-2}$ up $\approx 30 \times 10^{10} \text{ cm}^{-2}$ (p-type doping) for graphene on SiO_2/Si , and is also related to the impurity density of charges in SiO_2 [34]. As we can notice, even without the application of gate voltage, graphene has a residual charge density (n_0), which is added to the charge density provided through the application of gate voltage.

For a back gate voltage, considering the application of V_{bg} , the density of graphene charge carriers is given by:

$$n_t = n_0 + n_{V_g} = \frac{C_{ox}V_{bg}}{e} + n_0 = \frac{\epsilon_d \epsilon_0 V_{bg}}{de} + n_0, \quad 10$$

where n_{V_g} is the charge density acquired due to the application of a gate voltage, $C_{ox} = \epsilon_d \epsilon_0 / d$ is the capacitance per unit area for the graphene/insulator/Si structure (dielectric

capacitance), and d and ϵ_d are the thickness, as well as the dielectric constant of the insulator layer, respectively.

It is noteworthy that the quantum capacitance of graphene [35, 36, 37] can be neglected for values of the dielectric constant of the insulator $\epsilon_d \approx 4$, gate voltage bigger than a few millivolts, thickness of the insulator bigger than a few Angstroms. It is worth mentioning that, in the back voltage configuration, the thickness of the insulator is generally greater than 200 nm.

As in the back voltage configuration, the electric field has a low value it is necessary to apply large potential differences (PD) to obtain moderate increments of charge density. On the other hand, the application of high PD values ($PD > 100$ V) can cause damage to the insulator layer. Therefore, taking into account the above, we can affirm that the back gate voltage process is limited. To overcome this problem it is necessary to decrease the thickness of the insulator layer, but obtaining thinner layers of this dielectric requires more advanced techniques. Another solution is to use a dielectric with a high dielectric constant value, such as, for example, HfO_2 . However, the most used solution is the application of a top-gate voltage, according it is showed in Figure 5b.

In this top-gate structure, a graphene nanoribbon is deposited on silicon, and the insulator is deposited above the graphene, which is in contact with the electrode (“gate electrode”). An option to further increase the efficiency of the top-gate voltage is to replace SiO_2 with h-BN, the thickness of the h-BN layer being thin enough to increase the generation of charges in graphene (usually between 10 at 20 nm).

We used that gate voltage configuration in our devices because besides being more efficient, the intrinsic charge of graphene (+) is added to the charge generated by the gate voltage (positive too), which contributes to a lower applied voltage.

The Fermi level of graphene due to the applied voltage is given by [38]:

$$E_F \cong \mu_g = \pm \hbar V_F \sqrt{\frac{\pi \epsilon_0 \epsilon_d}{e h_d} |(V_g - V_D)|}, \quad 11$$

where $\epsilon_0 \epsilon_d$ is the electrical permittivity of the dielectric, h_d is the thickness of the dielectric (h-BN), and V_D is the Dirac voltage (We considered $V_D = 4.5$ V, $h_d = 10$ nm, and $\epsilon_d = 3.4$ in our calculations). Note that from Equation 11, considering $V_g = 0$, we can see that graphene has an intrinsic chemical potential $\mu_g \approx -0.161$ eV (p-doped).

It is importante to state, that there are different values in the international scientific literature regarding V_D . For example, a graphene film on SiO_2/Si presented a low Dirac voltage ($V_D < 4.5$ V, the average value of around 2.5 eV [38]). However, in an another

Research, where a graphene layer over h-BN/SiO₂/Si, was used, the Dirac voltage presented value $V_D \approx 5$ V. On the other hand, for graphene on SiO₂/Si the Dirac value was $V_D \approx 25$ V [39].

3. Graphene-based BPSK and QPSK modulators

Before we start detailing the modulators we are presenting, let's make an analytical comparison between the silicon-based modulators based on a traveling wave electrode and our modulators based on waveguides made of graphene.

The signal considered at the entrance of the MZM is given by $E_{in} = E_0 e^{j\omega t}$ and the signals that propagate in the two arms of the silicon MZMs (in the x-direction) are given by, $E_1 = E_0 e^{j(\omega t - k_{c1}x + \phi_0)}$; $E_2 = E_0 e^{j(\omega t - k_{c2}x + \phi_0)}$, where the complex wavenumber $k_c = \beta - j\alpha$, $\beta = 2\pi/\lambda$ is the phase constant (rad/m), λ is the wavelength of the propagating mode, α is the attenuation constant, and ϕ_0 is the initial phase. As ϕ_0 does not influence what is showed below, we disregard this parameter. Therefore, after the coupling of the two signals mentioned above (on the output coupler), then the resulting signal is given by (E_{out}):

$$E_{out} = E_1 + E_2 = \frac{1}{\sqrt{2}} E_0 e^{-\alpha x} (e^{j(\omega t - \beta_1 x)} + e^{j(\omega t - \beta_2 x)}). \quad 12$$

Then, considering the input signal with cosine shape, the output signal is given by:

$$E_{out} = \frac{1}{\sqrt{2}} E_0 e^{-\alpha x} (1/2)[\exp(j(\phi_1)) + \exp(-j(\phi_1))] + (1/2)[\exp(j(\phi_2)) + \exp(-j(\phi_2))], \quad 13$$

where $\phi_1 = \omega t - \beta_1 x$ e $\phi_2 = \omega t - \beta_2 x$.

As an example, we are showing the graphics referring to the behavior of the phases of the MZM output signal as a function of time, regardless of attenuation, (concerning E_{in}),

in Figure 6, considering $\beta_{1x} = 45^\circ$, $\beta_{2x} = 90^\circ$ rad, $\beta_{2x} = 135^\circ$, and $\beta_{2x} = 225^\circ$, for $\lambda_0 = 1.55052 \mu\text{m}$ (one of the ITU-T band C wavelengths, in the air).

(Figure 6)

Note that in these cases, the MZM output signals are out of phase related to the input signal by $\phi = 45^\circ$, 90° , and 180° (destroyed), respectively. Also, note that although we are only interested in phase modulation, the output signal also has amplitude modulation.

We considered $\beta_{1x} = 45^\circ$ just to show the theory involved in this subject. However, in silicon MZMs, usually, $\beta_{1x} = 90^\circ$ since, in this way, the MZM output signals have more symmetrical lags concerning the input signal.

It is worth mentioning that, in general, the reverse voltage values for the modulator signals applied in silicon-based MZMs are determined experimentally.

Without loss of generality, we considered a monochromatic cosine signal continuous wave (CW) laser to simplify the technical details of the modulator we are presenting. Therefore, the output signal, considering only a waveguide with length L_w , is given by:

$$E_{out} = E_{inp} e^{\frac{-\alpha L_w}{2}} e^{j(\omega t - \beta L_w)} \quad 14$$

In Figure 7, we are showing the schematic representation of the modulator we are presenting. As we can see this modulator consists of only one waveguide embedded in an h-BN insulating layer, supported by a silicon substrate. Indeed, the waveguide is a graphene nanoribbon with length L_w embedded in h-BN, the top layer having a thickness of 10 nm, and the bottom layer 20 nm. The gate voltage system consists of a metal electrode/graphene/h-BN junction.

(Figure 7)

We can obtain the phase shift between the input and output signals by varying the complex wavenumber using a gate voltage. Thus, we obtained the phase shifts, as well as the optical losses suffered by the optical signal that propagates inside the waveguide, through the complex wavenumber referring to the GSPP mode in the direction of its propagation. In this graphene-based modulator, non-linear effects were not considered,

since the amplitude of the inserted optical signal is chosen, so that these effects are avoided [40].

Taking into account that we will obtain the phase shift in the spatial domain, the phase difference $\Delta\phi$ between the waveguide output signal (which suffers delay) and the inserted signal is given by:

$$\Delta\phi = \beta L_w. \quad 15$$

Therefore, we can get the same phase as the inserted signal, considering $\beta L_w = n2\pi$, where n is an integer, i.e., the number of periods (in the spatial domain) between the input and output signals.

Notice, in Figure 7, that for the device we are presenting to operate as a phase modulator, firstly, we should insert a continuous voltage (DC) into the graphene, which works as a waveguide. This voltage (gate voltage) determines the chemical potential necessary for obtaining the real part of the complex wavenumber for GSPP TM modes.

As we can see, it is shown the real and imaginary parts of K_c as a function of the graphene's chemical potential ($0.5 \text{ eV} \leq \mu_g \leq 0.8 \text{ eV}$; $\lambda_0 = 1.55052 \text{ }\mu\text{m}$), in the left part of Figure 8.

(Figure 8)

We also plotted the graph regarding the propagation length, i.e., $L_p = 1/2 \text{ Imag}(k_c)$ versus μ_g , for the same range of values mentioned above (right part of Figure 8). Hence, we have adopted the value $\mu_g = 0.65 \text{ eV}$ and found $L_p \approx 396 \text{ nm}$, which is sufficiently greater than the value of the length of the waveguide that we adopted ($L_w = 50.061 \text{ nm}$), as we will show further.

We used the parameters mentioned above for the initial operation of the modulator and we applied the changing of the chemical potential, using the electrical modulator signal, to provide the desired phases of the output signal, as shown in Figure 8. It is noteworthy that we also found, numerically, the values referring to the maximal propagation length (L_{pm}) that GSPPs modes can propagate, with attenuation within the acceptable limit. Therefore, we can be sure that the output signal suffers no attenuation, i.e., it will have sufficient amplitude.

For our device to work as a BPSK modulator, we determined the DC gate voltage, number of atoms in the propagation direction, length of the waveguide, maximal propagation length, number of periods, graphene chemical potential due to the electrical modulator signal, and gate voltage needed for the electrical modulator signal: $V_b =$

12.016; $N_a = 407$; $L_w = 50.061$ nm; $L_{wm} = 345.17$ nm; $N_p = 17$, $\mu_{g2\pi} = 0.644$ eV; $V_{2\pi} = -0.313$ V, $\mu_{g\pi} = 0.638$ eV; $V_{\pi} = -0.621$ V, respectively (for TM modes).

It is worth mentioning that we determined the gate voltage values from Equation 11.

It is relevant to state that N_p is applied to all periods in the temporal domain related to a bit of that modulated signal, taking into account the duration time of one bit of the modulator signal.

Concerning the resistance of graphene, as a function of the applied voltage, a graphene nanoribbon can withstand voltages up to the value that causes its breakdown current density, that is, (10^8 A/cm²) [41], therefore much higher than the values we used.

Another great advantage of graphene is the possibility of using the signal to be modulated in the THz frequency range. For example, considering the frequency 50 THz ($\lambda_0 = 5.99585$ μ m) for the signal to be modulated, the values for the chemical potential due to the DC gate voltage, that DC voltage, number of atoms in the propagation direction length of the waveguide, maximal propagation length, number of periods, graphene chemical potential due to the electrical modulator signal, and gate voltage needed for the electrical modulator signal are: $\mu_{gb} = 0.2$ eV; $V_b = -2.936$ V; $N_a = 1220$; $L_w = 150.06$ nm; $L_{wm} = 211.52$ nm; $N_p = 9$, $\mu_{g2\pi} = 0.195$ eV; $V_{2\pi} = -0.078$ V, $\mu_{g\pi} = 0.19$ eV; $V_{\pi} = -0.153$ V, respectively (for TM modes).

However, the main advantage regarding the modulator we are presenting is the fact that it can also operate as a QPSK modulator. That is because changing the complex wavenumber of graphene via gate voltage makes it possible, in an efficient way, the 45°, 135°, 225°, and 315° phases (referring to dibits 00, 01, 11, and 10, respectively) without the need for obtaining the phase difference between two BPSK signals, i.e., without the need for a thermo-optic (TO) phase shifter.

Using the same length as the waveguide used in the BPSK modulator, we determined the parameters for this QPSK modulator (for $\lambda_0 = 1.55052$ μ m): $L_{pm} \approx 313$ nm; $N_a = 407$; $L_w = 50,061$ nm; to obtain $\phi = \pi/4$ ($\mu_{g\pi/4} = 0.642$ eV, $V_{\pi/4} = -0.392$ V); to obtain $\phi = 3\pi/4$ ($\mu_{g3\pi/4} = 0.639$ eV, $V_{3\pi/4} = -0.546$ V); to obtain $\phi = 5\pi/4$ ($\mu_{g5\pi/4} = 0.636$ eV, $V_{5\pi/4} = -0.695$ V); to obtain $\phi = 7\pi/4$ ($\mu_{g7\pi/4} = 0.633$ eV, $V_{7\pi/4} = -0.837$ V), for TM modes.

It is noteworthy that the application of $V_{\pi/4}$ occurs for bits "00" V_{π} for bits "01" and $V_{5\pi/4}$ for bits "11", and $V_{7\pi/4}$ for bits "10", as we can see by Figure 7. Note, also, that in both cases, occurs very small attenuations.

To prove what is detailed above, we plotted two periods related to the amplitude versus time (Equation 14), for $x = 0$ and $x = L_w$. We considered $E_0 = 1$ V (this value has been selected only to simplify the calculations), referring to the application of E_{in} and the amplitude for V_π ($k_{cv\pi} = 2.196439621844192 \times 10^9 + 1.444759823745566 \times 10^6i$), to prove what is detailed above, as we can see in Figure 9.

(Figure 9)

Complementing this subject, as the phase difference in the air (as a function of the propagation distance, considering the spectral domain), is given by $\phi_a = k_0L_a$ (where L_a is the propagation distance in the air), and in the waveguide is given by $\phi_g = \text{real}(k_{cg})L_g$ (where L_g is the propagation distance in the waveguide), it is easy to see, that $\phi_g = \phi_a \text{real}(k_{cg})L_g / k_0L_a$. So, for example, considering that the wavelength in the waveguide is half the value of the wavelength in the air, to obtain a phase difference $\Delta\phi = \pi$, between the wave propagating in the air and the wave propagating in the waveguide, the waveguide length must be $L_w = 1.16289 \mu\text{m}$, considering only a period of the wave propagating in the air.

In the data reported above, we opted for the strict control of the gate voltage to obtain the necessary values for each phase change. It is noteworthy that our QPSK modulator can also operate in the TeraHertz range.

The graphene-based modulator we are presenting has enormous advantages over conventional silicon modulators that operate through PN-junction rib-waveguide phase shifters. Note that in addition to the system being much simpler, it is cheaper, as only a waveguide and the gate voltage system are used. Furthermore, the signal modulation is much faster because, in the TWE, it is necessary, the movement of electrical charges via diffusion, in part of the operation, for the alteration of the refractive index through the modulator signal. On the other hand, in our device, we get the phase modulation by loading of the capacitive system graphene/h-BN/metallic electrode. Hence, the bit rate can be much higher than what silicon modulators can handle. Indeed, concerning the modulators that we are currently presenting, that transmission rate is limited by the speed of current electronic devices. It is worth mentioning that obtaining modulating signals with a bit rate greater than 100 Gbps is still a challenge. However, this bit rate evolved from 2.5 Gbps [40] in 2003 to more than 100 Gbps, between 2003 and 2010, and in 2010, bipolar SiGe transistors providing 500 GHz were already being researched, using BiCMOS technology (bipolar and MOS technology on the same chip) [42, 43]. As new

technologies are emerging, we can say that the transmission rate in the Terabits range is possible.

In experiments on graphene field-effect transistor, the source and drain electrodes were manufactured by electron-beam lithography and thermal evaporation of the metals, with Au (50 nm thick) and Ti (5 nm thick), with resistance less than a few k Ω . For the gate voltage electrode, the aluminum electrode was 30 nm thick and was deposited directly on graphene. However, it was found that between graphene and the electrode a natural insulator appeared after that device was exposed to the air for several hours [44]. This natural oxide, with a dielectric constant between 5 and 9, as well as the thickness between 5 and 9 nm, was used as a insulating layer between the electrode and graphene. We can use this aluminum electrode to apply the gate voltage over the h-BN, but in our case, this natural oxide must be avoided to improve the efficiency of the gate voltage system using h-BN as the insulation layer.

4. Conclusions

We are presenting a graphene-based BPSK and QPSK modulators, which can operate from the TeraHertz range, to the infrared and has enormous advantages over the silicon modulators with lateral PN-junction rib-waveguide phase shifters. For example, these graphene modulators have only a much simpler waveguide and gate voltage application system than those used in silicon-based MZMs. Besides, they are more efficient, cheaper, and have shorter lengths (and consequently, greater integration in photonic integrated circuit (PIC)).

In this manuscript, we first detailed the issues relating to the theory involving silicon MZMs and graphene, which is need to detailing of the modulator we are presenting. After this step, we show the project, numerical simulations, and analyzes concerning this device.

We believe that this modulator is part of the new generation of devices made up of 2D materials, which should revolutionize this area of science.

Financial and Ethical disclosures

Funding: This study was funded by Cearense Foundation for Scientific and Technological Development Support - FUNCAP (grant number DCR-0024-00026.03.00/15) and National Council for Scientific and Technological Development – CNPq (grant number 314915/2018-4).

Data Availability

The data that support the findings of this study are available from the corresponding author upon reasonable request.

References

- [1] K. Kikuchi, “Digital coherent optical communication systems: fundamentals and future prospects”, *IEICE Electronics Express*, Vol. 8, No. 20, 1642 – 1662, (2011).
- [2] R. Griffin and A. Carter, “Optical differential quadrature phase-shift key (oDQPSK) for high capacity optical transmission”, *Proc. Optical Fiber Communication Conference*, (2002).
- [3] K. Ogawa et al., “Design and characterisation of high-speed monolithic silicon modulators for digital coherent communication”, *Proc. of SPIE Vol. 9367*, 93670C (2015).
- [4] R. A. Soref, and B.R. Bennett, "Electrooptical Effects in Silicon," *IEEE J. Quantum Elect.*, vol. QE-23, pp. 123-129, (1987).
- [5] M. Nedeljkovic, R. Soref, and G. Z. Mashanovich, “Free-carrier electrorefraction and electro-absorption modulation predictions for silicon over the 1-14 um infrared wavelength range,” *IEEE Photonics J.* 3(6), 1171 – 1180, (2011).
- [6] T.-Y. Liow et., “Silicon Quadrature Phase-Shift-Keying Modulator for 40- and 100-Gb/s Transmission”, *Fujikura Technical Review*, (2014).
- [7] A. M. Gutierrez, “Analytical Model for Calculating the Nonlinear Distortion in Silicon-Based Electro-Optic Mach–Zehnder Modulators”, *Journal of Lightwave Technology*, Vol. 31, No. 23, (2013).
- [8] F. Koyama and K. Iga, “Frequency chirping in external modulators,” *J. Lightwave Technol.* 6(1), 87-93, (1988).
- [9] K. Goi, K. Oda, H. Kusaka, Y. Terada, K. Ogawa, T.-Y Liow, X. Tu, G.-Q Lo and D.-L Kwong, “11-Gb/s 80-km transmission performance of zero-chirp silicon Mach-Zehnder modulator,” *Opt. Exp.* 20(26), B350-B356 (2012).
- [10] K. Ogawa, “High-speed silicon-based integrated optical modulators for optical-fiber telecommunications,” *Proc. SPIE 8990*, 8990-1-8990-8 (2014).
- [11] G. T. Reed, G. Mashanovich, F. Y. Gardes, and D. J. Thomson, “Silicon optical modulators,” *Nat. Photon.*, Vol. 4, No. 8, pp. 518-526, (2010).
- [12] C. H. Gan, H. S. Chu and E. P. Li, “Synthesis of highly confined surface plasmon modes with doped graphene sheets in the mid-infrared and terahertz frequencies”, *Phys. Rev. B* 85, 125431 – 9 pages, (2012).

- [13] L. A. Falkovsky and S. S. Pershoguba, “Optical far-infrared properties of a graphene monolayer and multilayer”, *Physical Review B* 76, 153410 (2007).
- [14] X. Luo, T. Qiu, W. Lu, Z. Ni, “Plasmons in graphene: Recent progress and applications”, *Elsevier - Materials Science and Engineering: R: Reports*, Vol. 74, Issue 11, pp. 351-376, pp. 351–376, (2013).
- [15] B. Wang, X. Zhang, X. Yuan, and J. Teng, “Optical coupling of surface plasmons between graphene sheets”, *Applied Physics Letters* 100, 131111 (2012).
- [16] A. Vakil and Nader Engheta, “One-Atom-Thick IR Metamaterials and Transformation Optics Using Graphene”, *Cornell University Library*, arXiv:1101.3585v1, (2011).
- [17] A. J. Wirth-Lima, P. P. Alves-Sousa and W. Bezerra-Fraga, “Graphene’s photonics and optoelectronics properties – A Review”, *Chinese Physics B*. Vol. 29, No. 3, 037801, (2020).
- [18] C. R. Dean, A. F. Young, I. Meric, C. Lee, L. Wang, et al., “Boron nitride substrates for high-quality graphene electronics”, *Nature Nanotechnology* 5, pp. 722 – 726, (2010).
- [19] A. Laturia, M. L. Van de Put and W. G. Vandenberghe, “Dielectric properties of hexagonal boron nitride and transition metal dichalcogenides: from monolayer to bulk”, *2D Materials and Applications*, Volume 2, 6, (2018).
- [20] J. Wang, F. Ma and M. Sun, “Graphene, hexagonal boron nitride, and their heterostructures: properties and applications”, *RSC Adv.*, 7, 16801, (2017).
- [21] S. A. Mikhailov and K. Ziegler K, *Phys. Rev. Lett.* 99 016803, (2007).
- [22] Z. Lei, F. Xiu-Li, L. Ming, C. Jian-Jun, Y. Jun-Zhong, P. Zhi-Jian e T. Wei-Hua, “Coupling interaction between a single emitter and the propagating surface plasmon polaritons in a graphene microribbon waveguide”, *Chin. Phys. B*, Vol. 23, No. 3, 03810, (2014).
- [23] F. Schedin, E. Lidorikis, A. Lombardo, V. G. Kravets, A. K. Geim, A. N. Grigorenko, K. S. Novoselov and A. C. Ferrari, *ACS Nano* 4 5617, (2010).
- [24] J. Christensen, A. Manjavacas, S. Thongrattanasiri, F. H. L. Koppens, and F. J. G. de Abajo, “Graphene Plasmon Waveguiding and Hybridization in Individual and Paired Nanoribbons”, *American Chemical Society*, Vol. 6, No. 1, pp. 431–440, (2012).
- [25] J. Xue, J. Sanchez-Yamagishi, D. Bulmash, et al., *Nat. Mater.* 10, 282, (2011).

[26] S. Goniszewski¹, M. Adabi, O. Shaforost, S. M. Hanham, L. Hao and N. Klein, “Correlation of p-doping in CVD Graphene with Substrate Surface Charges”, Scientific Reports, 6:22858, DOI: 10.1038/srep22858, (2016).

[27] Nistor, R. A., Kuroda, M. A., Maarouf, A. A. & Martyna, G. J. Doping of adsorbed graphene from defects and impurities in SiO₂ substrates. Phys. Rev. B 86, 041409, (2012).

[28] Moser, J., Verdaguier, A., Jimenez, D., Barreiro, A. & Bachtold, A., “The environment of graphene probed by electrostatic force microscopy”, Appl. Phys. Lett. 92, 123507, (2008).

[29] K. Tsukagoshi, H. Miyazaki, S.-L. Li, A. Kumatani, H. Hiura and A. Kanda, “Gate-Voltage Modulation in Graphene”, Chapter 11, “Graphene and its fascinating attributes”, World Scientific Publishing Co. Pte. Ltd., ISBN-10 981-4329-35-5, (2011).

[30] F. T. Vasko and I. V. Zozoulenko, “Conductivity of a graphene strip: Width and gate-voltage dependencies”, Appl. Phys. Lett. 97, 092115 (2010).

[31] Wirth-Lima, A.J., Alves-Sousa, P.P. and Bezerra-Fraga, W., Graphene’s photonic and optoelectronic properties – A review, Chin. Phys. B Vol. 29, No. 3, 037801, (2020).

[32] Lafkioti, M. et al., “Graphene on a hydrophobic substrate: doping reduction and hysteresis suppression under ambient conditions”, Nano Lett. 10, 1149–1153, (2010).

[33] Kong, J. et al., “Nanotube molecular wires as chemical sensors”, Science 287, 622–625, (2000).

[34] E. Pince and C. Kocabas, “Investigation of high frequency performance limit of graphene field effect transistors”, Appl. Phys. Lett., 97, 173106, (2010).

[35] J. Xia, F. Chen, J. Li and N. Tao, “*Measurement of the quantum capacitance of graphene*”, Nature Nanotechnology, Vol. 4, pp. 505 – 509, doi: 10.1038/nnano.2009.177, (2009).

[36] Arya Raj K. and Bala Tripura Sundari B., “Compact graphene field effect transistor modeling with quantum capacitance effects”, ARPN Journal of Engineering and Applied Sciences, Vol. 11, No. 2, (2016).

[37] S. Das Sarma, S. Adam, E. H. Hwang and E. Rossi, “Electronic transport in two-dimensional graphene”, Rev. Mod. Phys. 83, 407, (2011).

[38] Xu F, Das S, Gong Y, Liu Q, Chien H C, Chiu H Y, Wu J and Hui R, “Complex refractive index tunability of graphene at 1550nm wavelength”, Applied Physics Letters, 106, 031109, (2015).

[39] Kayyalha M and Chen Y P, “Observation of reduced 1/f noise in graphene field effect transistors on boron nitride Substrates”, *Applied Physics Letters* 107, 113101, (2015).

[40] Almir Wirth Lima Jr., João Cesar Moura Neto and Antonio Sergio Bezerra Sombra, “Attenuations, Dispersions and Nonlinearities in Graphene-Based Waveguides”, *Beilstein J. Nanotechnol.*, 6, 1221-1228, doi: 10.3762/bjnano.6.125, (2015).

[41] R. Muralia, Y. Yang, K. Brenner, T. Beck and J.D. Meindl, “Breakdown current density of graphene nanoribbons”, *Appl. Phys. Lett.* 94, 243114, (2009).

[42] J. Riishøj, 2.5 Gb/s laser-driver GaAs IC, *Journal of Lightwave Technology*, 11(7), 1139-1146, (1993).

[43] M. Möller, High-speed electronic circuits for 100 Gb/s transport networks, 2010 Conference on Optical Fiber Communication (OFC/NFOEC), pp. 1-3, (2010).

[44] H. Miyazaki, S. Li, A. Kanda and K. Tsukagoshi, *Semiconductor Science and Technology* 25, 034008 (2010).

Figure Captions

Figure 1: Figure 1: Top - Schematic representation of the MZM silicon. Bottom - A Cross-section of a silicon phase shifter, where the equivalent circuit of the PN junction, as well as the traveling wave electrode, are showed.

Figure 2: Schematic representation of the push-pull operation, related to a conventional silicon QPSK MZM.

Figure 3: Atomic structure of graphene, where we can see the distances between carbon atoms.

Figure 4: a) Real part of the graphene dielectric constant versus wavelength ($1.36 \mu\text{m} \leq \lambda \leq 1,625 \mu\text{m}$; $\mu_g = 0.55 \text{ eV}$). b) Imaginary part. c) Real part of the graphene dielectric constant versus chemical potential ($0.3 \text{ eV} \leq \mu_g \leq 0.9 \text{ eV}$; $\lambda = 1.55 \mu\text{m}$). d) Imaginary part.

Figure 5 (adapted from ref. [31]): a) Back gate voltage between a highly doped silicon substrate and a graphene nanoribbon. b) Top gate voltage between an electrode and a graphene nanoribbon.

Figure 6: $\text{Cos}(\phi)$ versus t for the signal in the air, $\phi = 45^\circ$, $\phi = 90^\circ$, and $\phi = 180^\circ$.

Figure 7: Schematic representation of the modulator consisting of electrode/graphene/h-BN metal used in the BPSK and QPSK modulators we are presenting.

Figure 8: Left side - Real and imaginary parts of the complex wavenumbers versus chemical potential of graphene ($0.5 \text{ eV} \leq \mu_g \leq 0.8 \text{ eV}$). Right side - Graph referring to the values of propagation length versus the chemical potential ($0.5 \text{ eV} \leq \mu_g \leq 0.8 \text{ eV}$).

Figure 9: Amplitude versus time with a phase difference $\Delta\phi = \pi$ in the air, and in the waveguide.

Figure 1

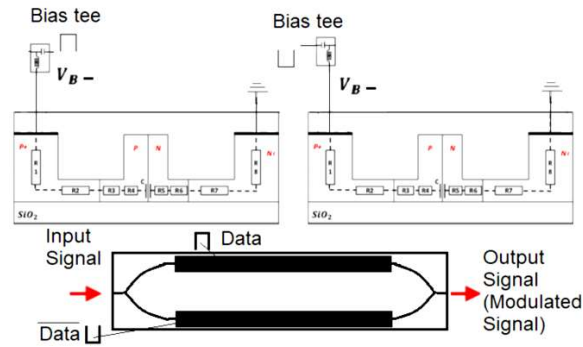


Figure 2

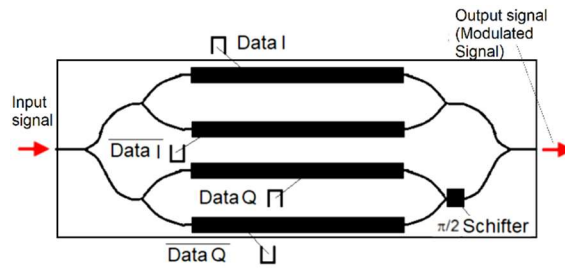


Figure 3

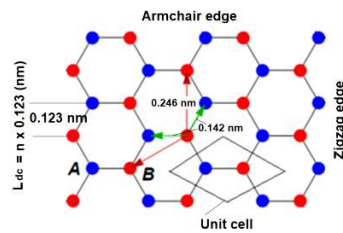


Figure 4

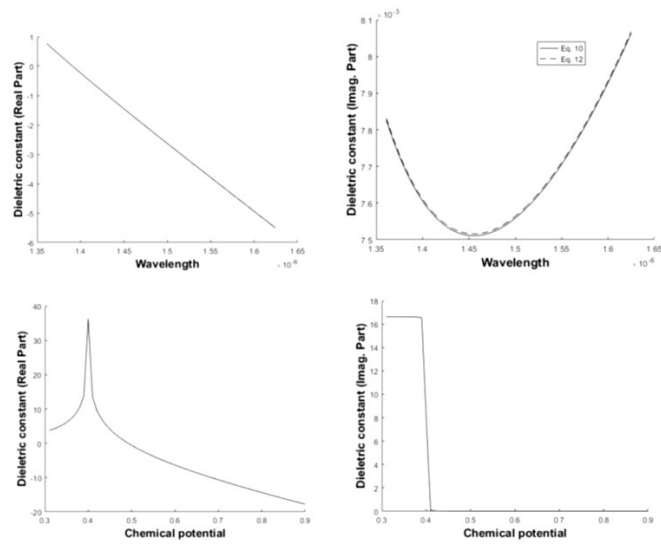


Figure 5

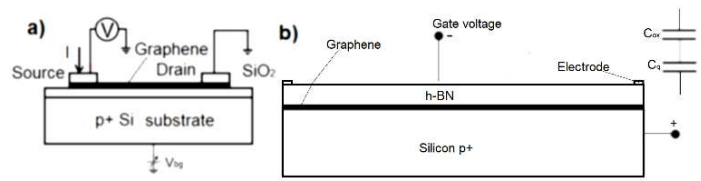


Figure 6

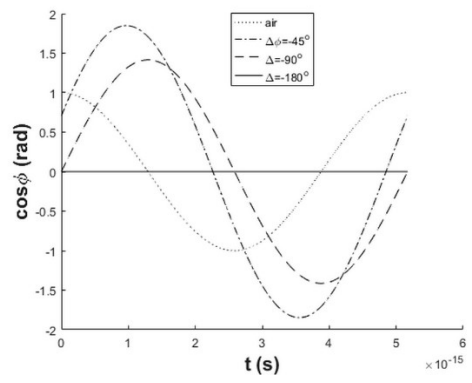


Figure 7

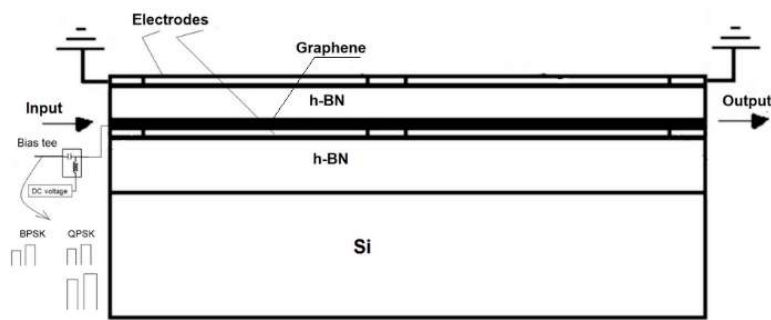


Figure 8

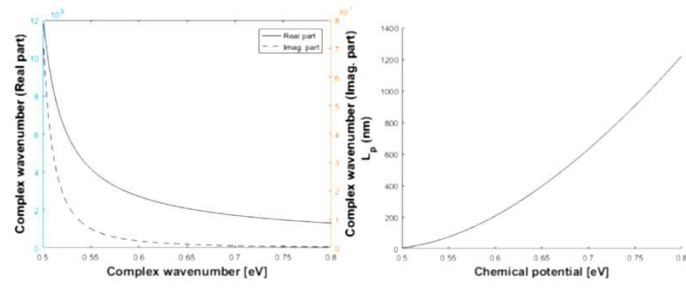
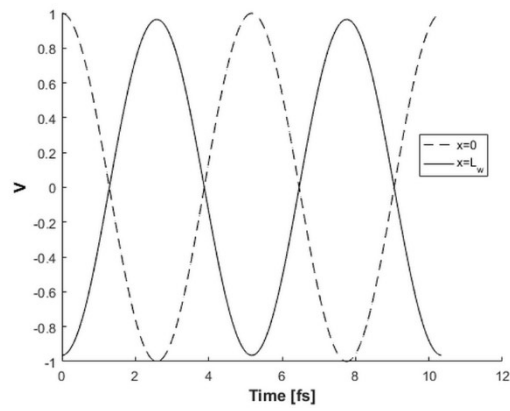


Figure 9



Figures

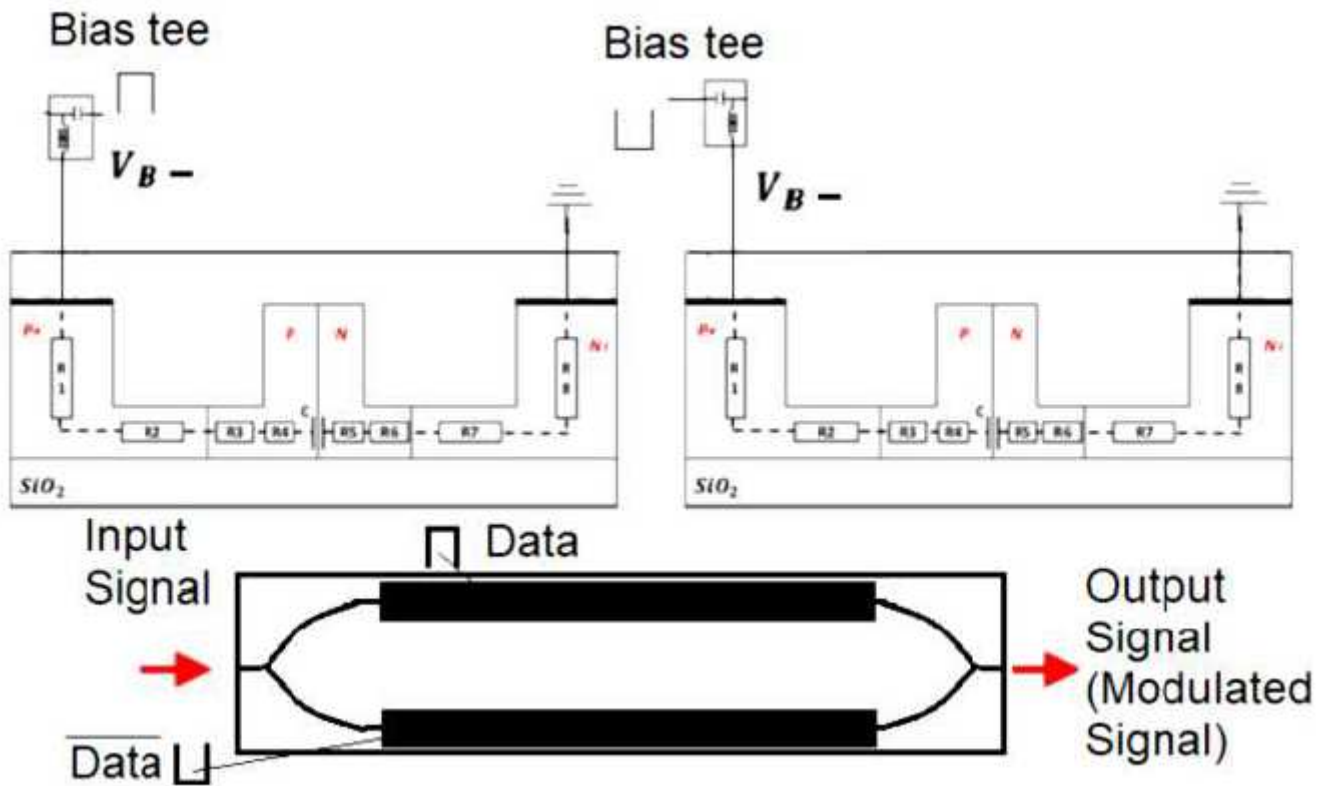


Figure 1

Top - Schematic representation of the MZM silicon. Bottom - A Crosssection of a silicon phase shifter, where the equivalent circuit of the PN junction, as well as the traveling wave electrode, are showed.

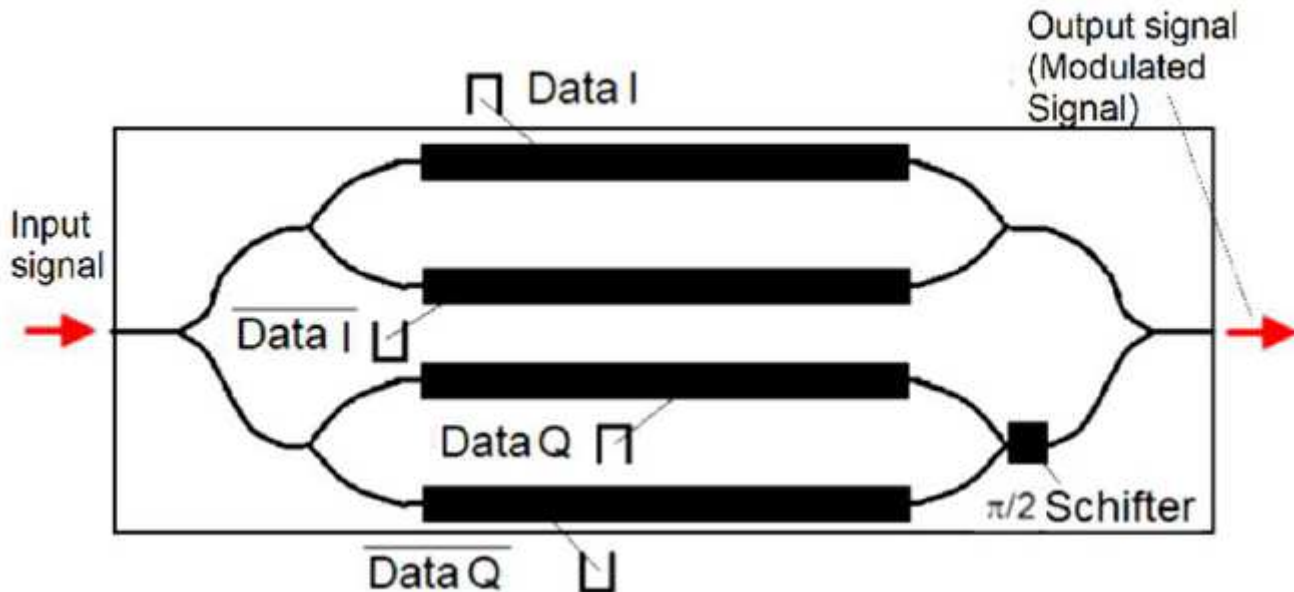


Figure 2

Schematic representation of the push-pull operation, related to a conventional silicon QPSK MZM.

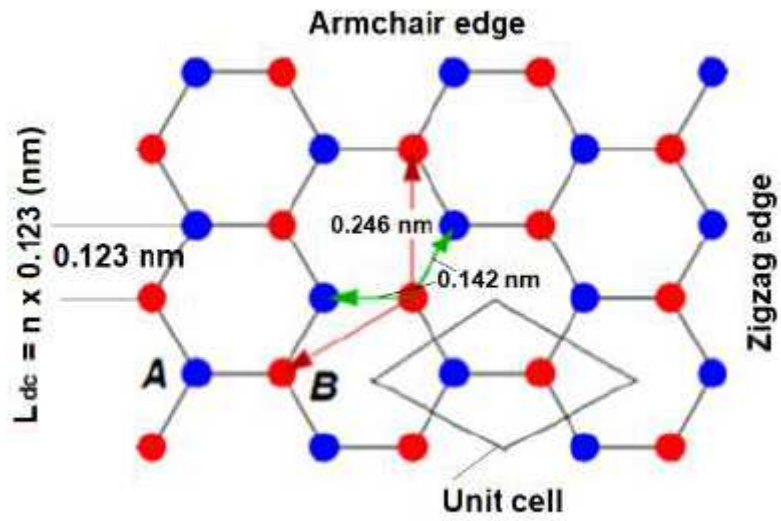


Figure 3

Atomic structure of graphene, where we can see the distances between carbon atoms.

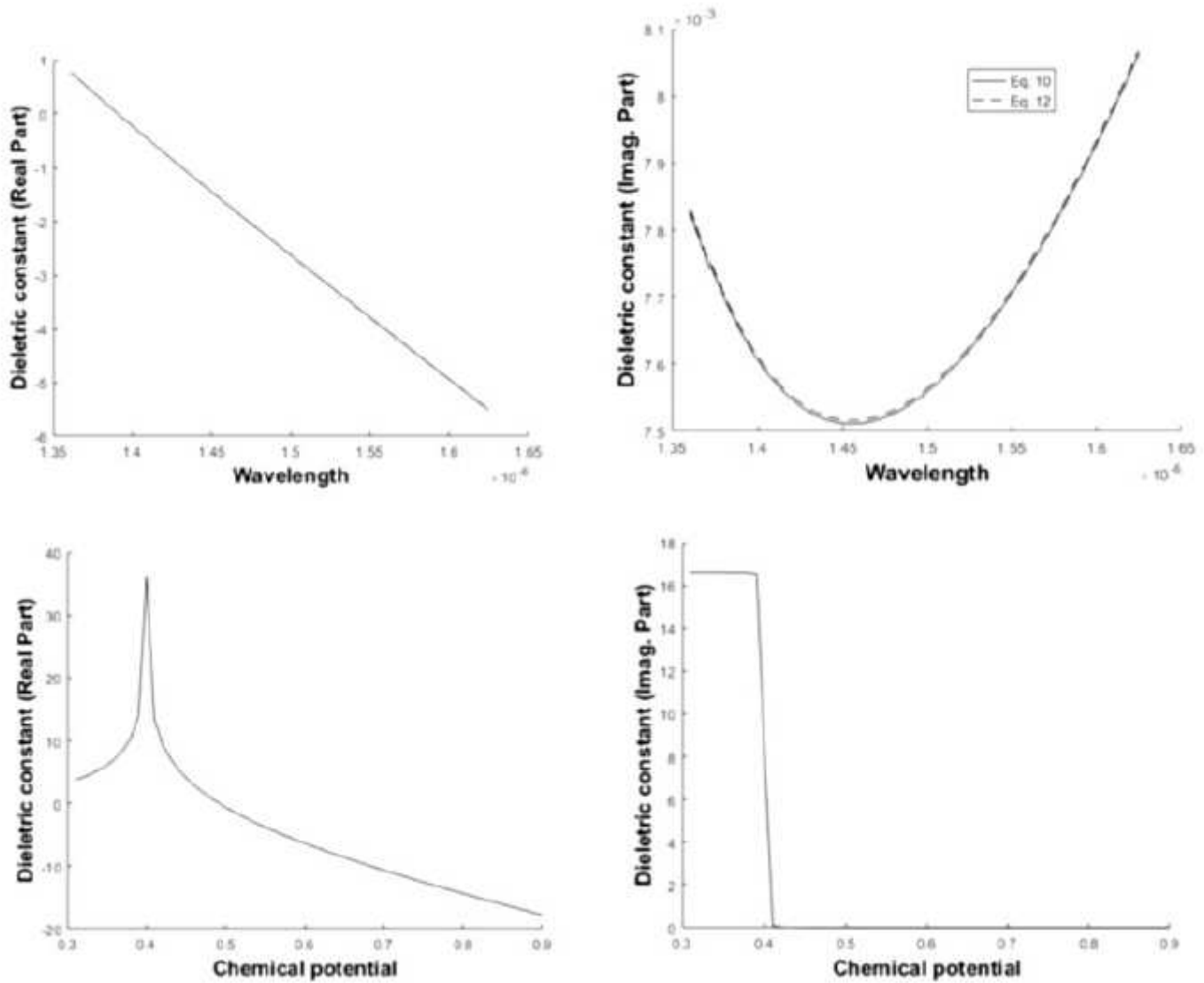


Figure 4

a) Real part of the graphene dielectric constant versus wavelength ($1.36 \mu\text{m} \leq \lambda \leq 1,625 \mu\text{m}$; $\mu\text{g} = 0.55 \text{ eV}$). b) Imaginary part. c) Real part of the graphene dielectric constant versus chemical potential ($0.3 \text{ eV} \leq \mu\text{g} \leq 0.9 \text{ eV}$; $\lambda = 1.55 \mu\text{m}$). d) Imaginary part.

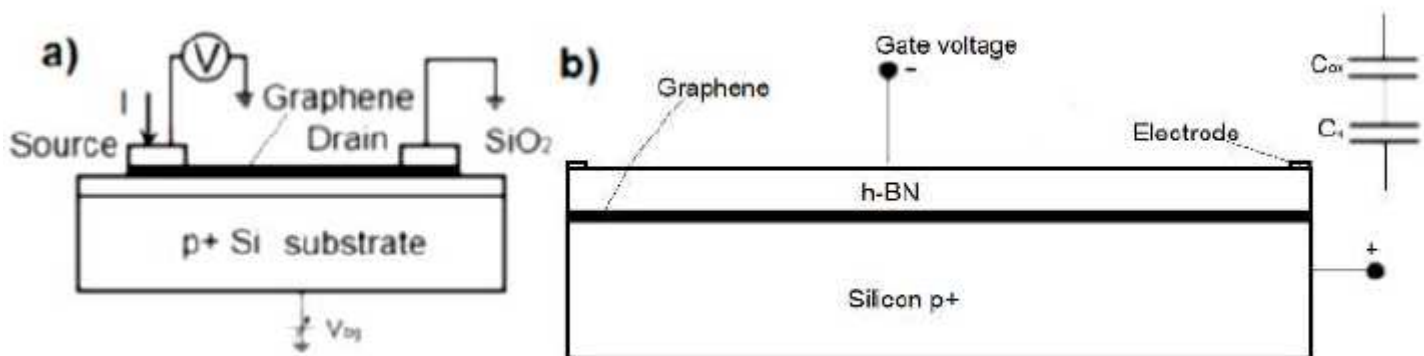


Figure 5

(adapted from ref. [31]): a) Back gate voltage between a highly doped silicon substrate and a graphene nanoribbon. b) Top gate voltage between an electrode and a graphene nanoribbon.

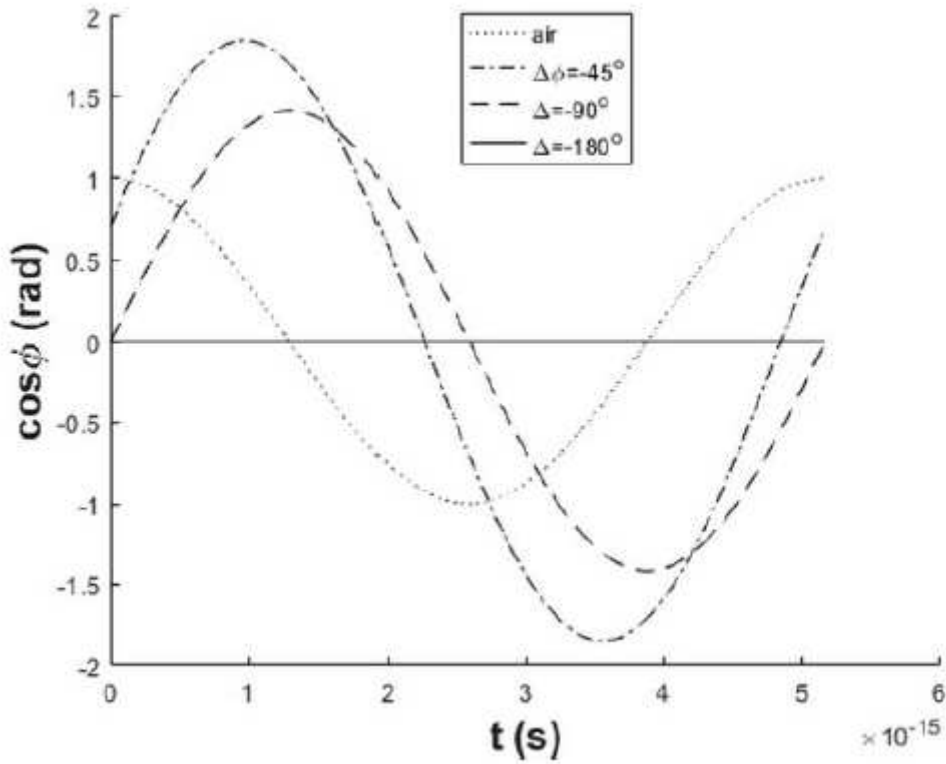


Figure 6

$\cos(\phi)$ versus t for the signal in the air, $\phi = 45^\circ$, $\phi = 90^\circ$, and $\phi = 180^\circ$.

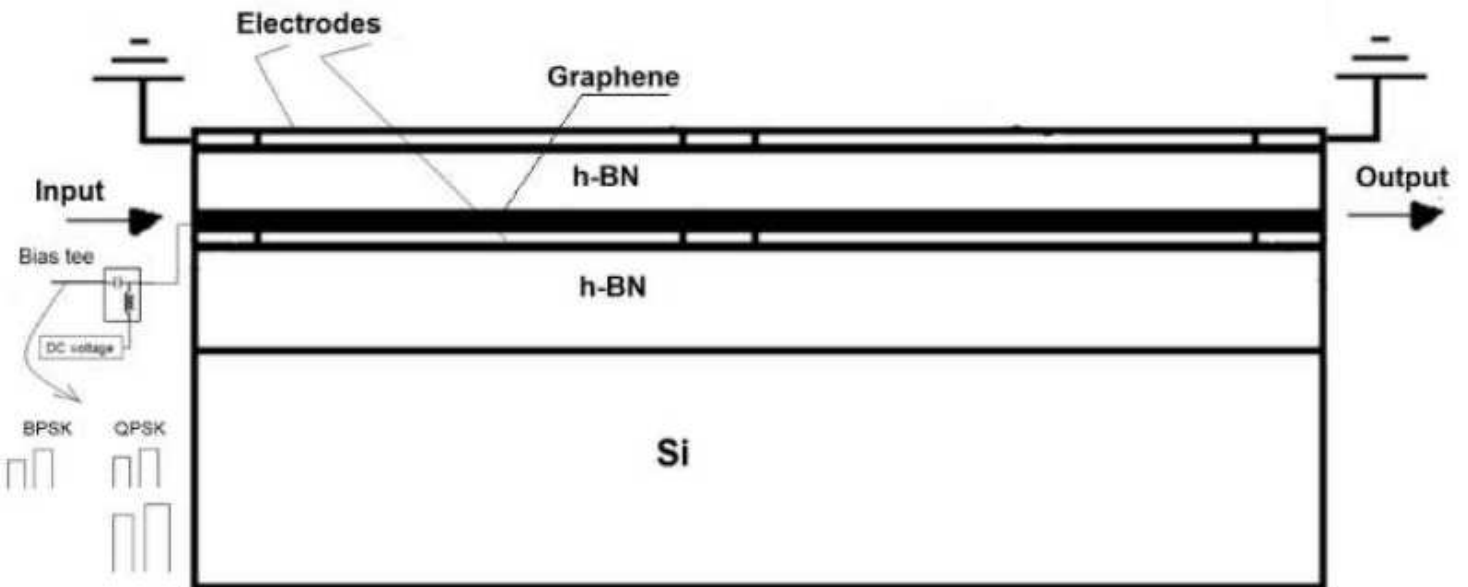


Figure 7

Schematic representation of the modulator consisting of electrode/graphene/h- BN metal used in the BPSK and QPSK modulators we are presenting.

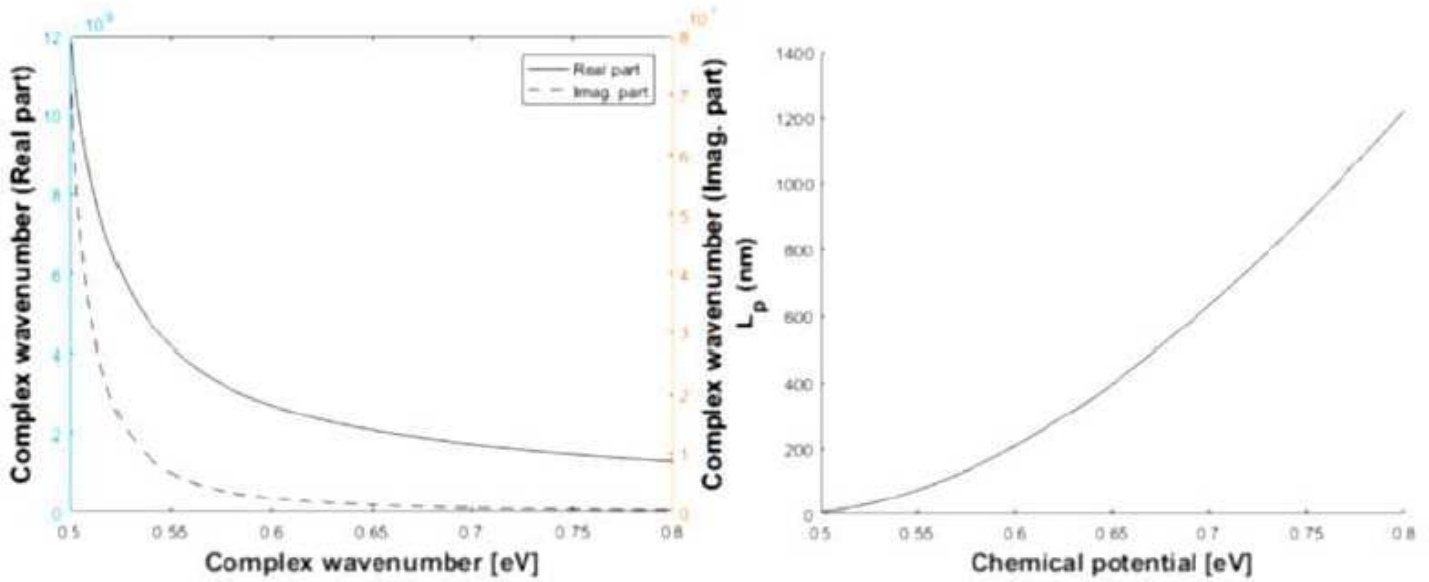


Figure 8

Left side - Real and imaginary parts of the complex wavenumbers versus chemical potential of graphene ($0.5 \text{ eV} \leq \mu_g \leq 0.8 \text{ eV}$). Right side - Graph referring to the values of propagation length versus the chemical potential ($0.5 \text{ eV} \leq \mu_g \leq 0.8 \text{ eV}$).

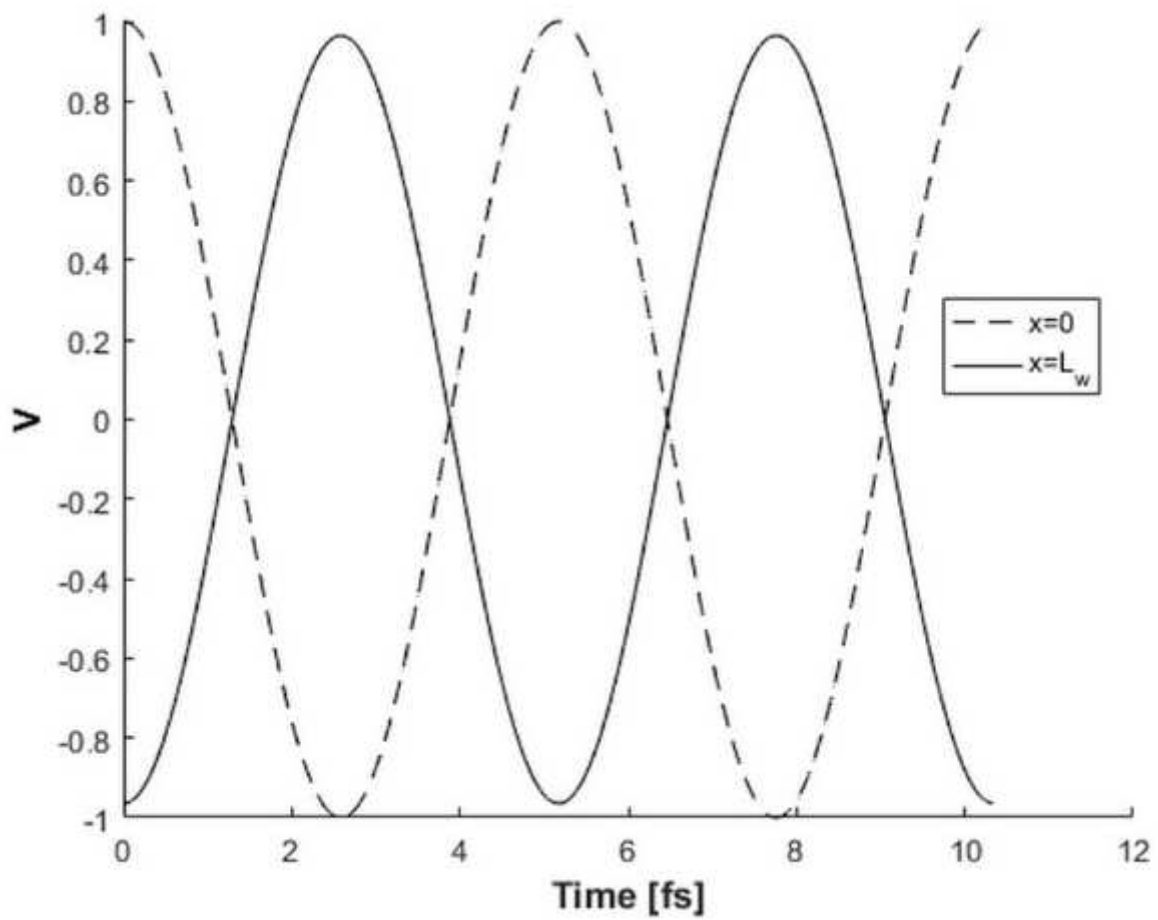


Figure 9

Amplitude versus time with a phase difference $\Delta\phi = \pi$ in the air, and in the waveguide.